Survey of nuclear pasta in the intermediate-density regime: Structure functions for neutrino scattering

B. Schuetrumpf,[1] G. Martínez-Pinedo,[1,2] and P.-G. Reinhard[3]

[1]*GSI Helmholzzentrum für Schwerionenforschung, Planckstraße 1, 64291 Darmstadt, Germany*

[2]*Institut für Kerphysik, Department of Physics, Technische Universität Darmstadt, Schlossgartenstraße 2, 64289 Darmstadt, Germany*

[3]*Institut für Theoretische Physik II, Universität Erlangen-Nürnberg, 91058 Erlangen, Germany*

(Received 22 December 2019; accepted 23 April 2020; published 18 May 2020)

Background: Nuclear pasta matter, emerging due to the competition between the long-range Coulomb force and the short-range strong force, is believed to be present in astrophysical scenarios, such as neutron stars and core-collapse supernovae. Its structure can have a high impact, e.g., on neutrino transport or the tidal deformability of neutron stars.

Purpose: We investigate the impact of nuclear pasta on neutrino interactions and compare the results to uniform matter.

Method: We calculate the elastic and inelastic static structure factors for nuclear pasta matter, using density functional theory (DFT), which contain the main nuclear input for neutrino scattering.

Results: Each pasta structure leaves a unique imprint in the elastic structure factor and it is largely enhanced. The inelastic structure factors are very similar for all configurations.

Conclusion: Nuclear pasta has a noticeable impact on neutrino neutral-current scattering opacities. While for inelastic reactions the cross section is reduced, the elastic coherent scattering increases dramatically. The effect can be of importance for the cooling of neutron stars as well as for core-collapse supernova models.

DOI: 10.1103/PhysRevC.101.055804

I. INTRODUCTION

Bulk matter with densities of about nuclear densities ($\rho_0 = 0.16\,\mathrm{fm}^{-3}$) is realized only in astrophysical objects, such as neutron stars or in supernova explosions. These sites are valuable laboratories, because nuclear matter properties, such as the nuclear equation of state, greatly impact such astrophysical scenarios.

Nuclear matter around saturation density is well described as uniform matter. However, at subsaturation densities nuclear matter clusters into a variety of intriguing shapes, commonly referred to as nuclear pasta. Nuclear pasta has been the topic of research for some decades [1,2] and has been much studied with classical [3,4] and quantum methods [5–17]. The impact of pasta matter on astrophysical objects is manifold: the viscosity of pasta matter can dampen the oscillations of neutron stars, its thermal conductivity is important for the neutron star cooling [18], it can explain the limitation of spin periods of pulsars [19], and its neutrino opacity has an impact on the early stage of cooling of the neutron star and the explodability of supernovae [20–25]. In this paper, we focus on neutrino scattering and the impact of pasta structures on neutrino opacities.

For neutrino scattering on uniform matter a large variety of studies can be found in the literature (e.g., [26–34]). They are mostly based on density functional theory or effective interactions and include in-medium particle correlations. These can have a significant impact on the opacities and thus on the astrophysical scenarios. For explicit nuclear pasta configurations the neutrino opacity has only been studied using the molecular dynamics (MD) framework [20–22,25]. MD has the advantage that it includes real particle-particle correlations between nucleons. However, the Pauli principle is only approximately realized by a phenomenological potential. These studies show an enhancement of neutrino scattering opacities due to coherent neutrino scattering.

In this work, we will employ nuclear density functional theory to calculate the structure factors of nuclear pasta, the main ingredients for the neutrino cross section. We will focus on the pasta configurations which appear at intermediate densities ($\rho_0/4$–$\rho_0/2$) which have been discussed in an earlier work [35]. In Sec. II, we introduce the pasta configurations and explain briefly the computation of neutrino scattering opacities and structure factors. In Sec. III, we present the results for the various nuclear pasta configurations and compare them to uniform matter.

II. NUCLEAR PASTA AND NEUTRINO SCATTERING

A. Minimal surfaces pasta configurations

In this work, we consider pasta configurations in the mid-density range, between 0.04 and 0.08 fm^{-3}. All configurations are related to minimal surfaces, which are the primitive (P), the gyroid (G), and diamond (D) surfaces [13,15,36]. Furthermore we also consider the flat or slab surface, which we label with (S). All these surfaces minimize the surface area locally and have a vanishing mean curvature. They can be characterized by the nodal approximations

$$\phi_S = \cos X, \tag{1a}$$

$$\phi_P = \cos X + \cos Y + \cos Z, \tag{1b}$$

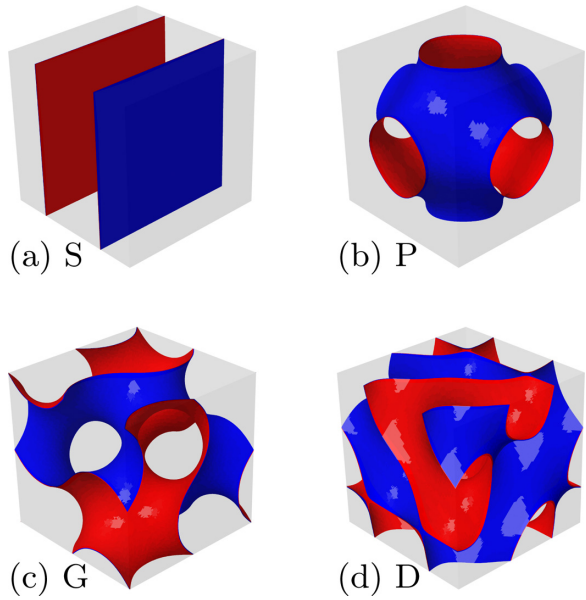

FIG. 1. One unit cell of minimal surfaces indicating the dividing surface between matter and vacuum: (a) slab, (b) P surface, (c) G surface, (d) D surface.

$$\phi_G = \cos X \sin Y + \cos Y \sin Z + \cos Z \sin X, \tag{1c}$$

$$\phi_D = \cos X \cos Y \cos Z + \cos X \sin Y \sin Z + \sin X \cos Y \cos Z + \sin X \sin Y \cos Z, \tag{1d}$$

where $X = 2\pi x/L$ and likewise for the other directions. L is the unit cell size. The condition $\phi_i = 0$ defines the surfaces which divide the space into two half spaces. They are illustrated in Fig. 1. One side is colored in red (light), the other in blue (dark). The division produces exactly two connected pieces. If one (e.g., $\phi_i > 0$) is filled with nuclear matter and the other remains (almost) void, then this is called a single configuration because the space filled with matter is singly connected. For the case of the gyroid, we also consider double configurations. Here either both half spaces are filled partly with nuclear matter ($|\phi_i| > t$) with a volume around the gyroid surface void. $t > 0$ is a filling parameter. We call this case the double gyroid networklike (dGn) configuration. The inverted case, where nuclear matter is located in the vicinity of the surface ($|\phi_i| < t$) is called the double Gyroid surfacelike configuration (dGs).

Simple models for the densities can be generated using the idealized dividing surfaces, Eq. (1), with

$$\rho^{(\mathrm{soft})}(\boldsymbol{r}) = \rho_0^{(\mathrm{soft})}[\phi_i(\boldsymbol{r}) - \phi_{i,\min}], \tag{2a}$$

$$\rho^{(\mathrm{hard})}(\boldsymbol{r}) = \rho_0^{(\mathrm{hard})}[\theta(\phi_i(\boldsymbol{r})) - \phi_0] \tag{2b}$$

with $i \in \{\mathrm{S}, \mathrm{P}, \mathrm{G}, \mathrm{D}, \mathrm{dGn}, \mathrm{dGs}\}$, $\theta(x)$ is the Heaviside theta function, and $\phi_{i,\min}$ the minimum value of $\phi_i(\boldsymbol{r})$. We adjust ρ_0 such that the desired mean density is reached. For the double surfaces we take the functions

$$\phi_{dGn} = +|\phi_G|, \tag{3a}$$

$$\phi_{dGs} = -|\phi_G|. \tag{3b}$$

TABLE I. Coupling constants taken from [27]. We take the values $\sin^2\theta_W = 0.23$ and $g_A = 1.26$.

Reaction	c_V	c_A
$\nu p \to \nu p$	$1/2 - 2\sin^2\theta_W$	$g_A/2$
$\nu n \to \nu n$	$-1/2$	$-g_A/2$

For the single structures we take $\phi_0 = 0$ and for the double gyroids we adjust ϕ_0 such that for half the box volume the density in nonzero.

The functions discussed above can be used as guiding potentials for nuclear ground state density functional theory (DFT) calculations in the Hartree-Fock framework using the Skyrme functional TOV-min which was developed to reproduce properties of nuclei and neutron stars [37]. Calculations were done in a periodic box on an equidistant grid using the SKY3D code from refs. [38,39]. All configurations were studied for proton fractions $X_P = 1/2$, $1/3$, and $1/10$ and mean densities between $\rho = 0.04$ and $0.08\ \mathrm{fm}^{-3}$ in steps of $0.01\ \mathrm{fm}^{-3}$. The lengths of the unit cells for the different shapes have been optimized to minimize the binding energy. Details of the ground state calculations can be found in [35].

B. Neutrino opacities

In this subsection, we briefly summarize the formalism of neutrino scattering on nuclear matter. More complete and detailed descriptions can be found, e.g., in [27,32,33].

In a neutron star environment neutrinos can be scattered elastically and inelastically on the nuclear matter. The opacity or cross section per volume for neutral-current scattering on a nonrelativistic gas of neutrons or protons is

$$\frac{1}{V}\frac{d^2\sigma(E_\nu)}{d(\cos\theta)\,dq_0} = \frac{G_F^2}{4\pi^2} n (E_\nu - q_0)^2 \big[c_V^2 (1+\cos\theta) S_V(q_0, \boldsymbol{q}) + c_A^2 (3 - \cos\theta) S_A(q_0, \boldsymbol{q})\big], \tag{4}$$

where G_F is the Fermi coupling constant, E_ν is the incoming neutrino energy, q_0 is the energy transfer, $\boldsymbol{q}$ is the momentum transfer, and θ is the scattering angle. n is the mean neutron or proton number density. The vector and axial coupling constants c_V and c_A are listed in Table I.

The only terms in Eq. (4) which depend on nuclear structure are the dynamic structure factors [32,33]

$$S_V(q_0, \boldsymbol{q}) = \frac{1}{2\pi n}\int dt\, e^{iq_0 t} \langle \Phi_0 | \hat{\rho}(t, \boldsymbol{q}) \hat{\rho}(0, -\boldsymbol{q}) | \Phi_0 \rangle, \tag{5a}$$

$$S_A(q_0, \boldsymbol{q}) = \frac{2}{3\pi n}\int dt\, e^{iq_0 t} \langle \Phi_0 | \hat{\boldsymbol{s}}(t, \boldsymbol{q}) \hat{\boldsymbol{s}}(0, -\boldsymbol{q}) | \Phi_0 \rangle. \tag{5b}$$

$|\Phi_0\rangle$ is the ground state wave function and

$$\hat{\rho}(0, \boldsymbol{q}) = \frac{1}{V}\sum_{i=1}^{N} e^{-i\boldsymbol{q}\cdot\boldsymbol{r}_i}, \tag{6a}$$

$$\hat{\boldsymbol{s}}(0, \boldsymbol{q}) = \frac{1}{V}\sum_{i=1}^{N} \hat{\boldsymbol{s}}_i e^{-i\boldsymbol{q}\cdot\boldsymbol{r}_i} \tag{6b}$$

are the Fourier transforms of density and spin-density operators, where $\hat{\mathbf{s}}_i$ the spin operator acting on the i neutron or proton. The time dependence of the operators is generated by propagating the operators (rather than the wave function) with the time-evolution operator of the DFT mean field. The structure factors are normalized such that $S(q \to \infty) = 1$.

The computation of the dynamic structure factors Eq. (5) requires either a fully time-dependent simulation or to resolve the full excitation spectrum of the system. However, for neutrino energies larger than the typical nuclear excitation energies of a few MeV, one can integrate out the dependence on q_0 in Eq. (4), yielding [33]

$$\frac{1}{V}\frac{d\sigma(E_\nu)}{d(\cos\theta)} = \frac{G_F^2}{4\pi^2} n E_\nu^2 \big[c_V^2(1+\cos\theta)S_V(\boldsymbol{q}) + c_A^2(3-\cos\theta)S_A(\boldsymbol{q})\big], \tag{7}$$

where

$$S_{V/A}(\boldsymbol{q}) = \int dq_0\, S_{V/A}(q_0, \boldsymbol{q}) \tag{8}$$

are the static structure factors. The gain is that the $S_{V/A}(\boldsymbol{q})$ can be determined solely from the ground state configuration, which is easier to compute.

The transport opacity is given by

$$\chi_T = \frac{\sigma_T}{V} = \int d(\cos\theta)\,\frac{d\sigma}{V d(\cos\theta)}(1-\cos\theta). \tag{9}$$

If we also average the cross section, Eq. (7), over the orientation of the incoming neutrino angle with respect to the pasta structure, we obtain

$$\chi_T(E_\nu) = \frac{2G_F^2 E_\nu^2}{3\pi} n\big[c_V^2\langle S_V(E_\nu)\rangle + 5c_A^2\langle S_A(E_\nu)\rangle\big] \tag{10}$$

with

$$\langle S_V(E_\nu)\rangle = \frac{3}{4}\int_{-1}^{1} dx\,(1-x^2)S_V(q), \tag{11a}$$

$$\langle S_A(E_\nu)\rangle = \frac{3}{20}\int_{-1}^{1} dx\,(1-x)(3-x)S_A(q), \tag{11b}$$

$$q = \sqrt{2E_\nu^2(1-x)}, \tag{11c}$$

where $x = \cos\theta$. The normalization ensures that the averaged structure factors are comparable. The factors in Eq. (10) emphasize that the axial part is about five times as strong as the vector part. $S_{V/A}(q)$ stand for the angular averaged structure factors. The total transport opacity is finally given as

$$\chi_T^{\text{tot}} = \frac{1}{\lambda_T} = \chi_{T,p} + \chi_{T,n}, \tag{12}$$

where n and p label neutrons and protons. The mean neutrino opacity is defined by averaging over the neutrino spectrum:

$$\left\langle \chi_T^{\text{tot}} \right\rangle = \langle 1/\lambda_T\rangle = \int \chi(E_\nu) f_\nu(E_\nu, T)\, E_\nu^2 dE_\nu, \tag{13}$$

where $f_\nu(E_\nu, T)$ is the neutrino distribution function for which we take a normalized Boltzmann distribution. In the above discussion we have considered neutral-current scattering but can be easily generalized to consider charged-current (anti)neutrino absorption reactions.

C. Static structure factors

As we have seen in the Sec. II B, the structure factors are the nuclear input to the scattering cross sections. The static structure factor of Eq. (8) can be expressed as [20]

$$S(\boldsymbol{q}) = \frac{1}{N}\sum_n |\langle\Phi_n|\hat{F}(\boldsymbol{q})|\Phi_0\rangle|^2, \tag{14}$$

with the sum running over excited states $|\Phi_n\rangle$. $\hat{F}(\boldsymbol{q})$ is the form factor operator that in isospin formalism can be expressed as

$$\hat{F}_{\text{tt}'}(\boldsymbol{q}) = \sum_{i=1}^{N} e^{i\boldsymbol{q}\cdot\boldsymbol{r}_i}\hat{T}_{\text{tt}'}, \tag{15a}$$

with the isospin selectors

$$\hat{T}_{nn} = \hat{T}_n = \frac{1+\hat{\boldsymbol{\tau}}_0}{2}, \quad \hat{T}_{pp} = \hat{T}_p = \frac{1-\hat{\boldsymbol{\tau}}_0}{2},$$
$$\hat{T}_{np} = \hat{\boldsymbol{\tau}}_+, \hat{T}_{pn} = \hat{\boldsymbol{\tau}}_-, \tag{15b}$$

where the $\boldsymbol{\tau}$ are standard isospin matrices. The form factor operators are not Hermitian, but obey the relation $\hat{F}^\dagger_{\text{tt}'}(\boldsymbol{q}) = \hat{F}_{\text{t}'\text{t}}(-\boldsymbol{q})$. We will abbreviate the diagonal part often as $\hat{F}_{\text{tt}} = \hat{F}_{\text{t}}$.

The static structure factors $S_{V/A}(\boldsymbol{q})$ can be decomposed into two parts: elastic and inelastic structure factors.

1. *Elastic structure factor*

The elastic vector structure factor includes only the contribution of the ground state in Eq. (14), and for a single unit cell it reads

$$S^{(0)}_{\text{el},t}(\boldsymbol{q}) = \frac{1}{N_t}|\langle\Phi_0|\hat{F}_t(\boldsymbol{q})|\Phi_0\rangle|^2. \tag{16}$$

Since our calculations respect time-reversal symmetry, the spin density is zero for the ground-state and hence the axial elastic structure factor is zero. Because our calculations are done for one elementary cell, we need to take the limit to infinite volume of the expression above. As the form factor scales with N_t, the number of particles of type t in the elementary cell, the heights of the elastic structure factor peaks still scale with N_t; however, the peaks become more narrow with increasing number of particles. Special attention has to be paid when performing the limit for an infinite system when the unit cell of the pasta configuration is repeated periodically. We consider here configurations which are perfectly periodic in all three space dimensions. Thus the form factor is only nonzero at the $\boldsymbol{k}$-space points $\boldsymbol{k}_\mu = 2\pi\boldsymbol{\mu}/L$, with $\boldsymbol{\mu} \in \mathbb{Z}^3$. Then the elastic structure factor becomes

$$S_{\text{el},t}(\boldsymbol{q}) = (2\pi)^3 n_t \sum_\mu \delta^3(\boldsymbol{q}-\boldsymbol{k}_\mu)\frac{1}{N_t}S^{(0)}_{\text{el},t}(\boldsymbol{k}_\mu), \tag{17}$$

where $\boldsymbol{k}_\mu$ are the reciprocal lattice vectors and $S^{(0)}_{\text{el},t}$ is the structure factor, Eq. (16), for one elementary cell. In the infinite limit, the elastic structure factor does not scale with

particle number, as in a finite system, but with the mean number density n_t.

The angular averaged structure factor, which is used to determine the neutrino opacity, becomes then

$$S_{\mathrm{el},t}(q) = 2\pi^2 n_t \sum_{\mu} \frac{\delta(q-k_\mu)}{q^2} \frac{1}{N_t^2} |\langle\Phi_0|\hat{F}_t(\boldsymbol{k}_\mu)|\Phi_0\rangle|^2. \quad (18)$$

2. Inelastic structure factor

The inelastic structure factor for a unit cell is determined as the elastic one in Eq. (16), but including excitations from the ground state to an excited state Φ_n:

$$S^{(0)}_{\mathrm{inel},tt'}(\boldsymbol{q}) = \frac{1}{N_t} \sum_{n>0} \langle\Phi_0|\hat{F}_{tt'}(-\boldsymbol{q})|\Phi_n\rangle\langle\Phi_n|\hat{F}_{t't}(\boldsymbol{q})|\Phi_0\rangle. \quad (19)$$

For the cell sizes and particle numbers considered here, finite size effects on the inelastic structure factor are small and our calculations represent already a very good approximation to the infinite system inelastic structure factor by taking $S_{\mathrm{inel},tt'}(\boldsymbol{q}) = S^{(0)}_{\mathrm{inel},tt'}(\boldsymbol{q})$.

If the spin-orbit interaction and thus the spin-mixing is small, the axial inelastic part can be approximated through the vector inelastic part. We have checked that this is a good approximation in our calculations and it will be used in the following. In summary, we have

$$S_{V,\mathrm{el},t} = S_{\mathrm{el},t}, \quad S_{V,\mathrm{inel},tt'} = S_{\mathrm{inel},tt'},$$
$$S_{A,\mathrm{el},t} = 0, \quad S_{A,\mathrm{inel},tt'} \approx S_{\mathrm{inel},tt'}. \quad (20)$$

3. Generalization to finite temperature

Both definitions of the structure factors, Eqs. (17) and (19), apply to zero temperature. At finite temperature, the system is described by a density operator $|\Phi_0\rangle\langle\Phi_0| \to \hat{D}_0$ for the thermal ground state. For a Slater determinant state $|\Phi_0\rangle$, $\hat{D}_0$ can be expressed as

$$\hat{D}_0 = \prod_{\alpha} \frac{\exp(-\hat{a}^\dagger_\alpha \hat{a}_\alpha \varepsilon_\alpha/T)}{1+e^{-\varepsilon_\alpha/T}}, \quad (21)$$

where T is the temperature and α runs over a complete set of single-particle states α. These are eigenstates of the mean-field Hamiltonian with single-particle energy ε_α. The detailed expressions for expectation values with $\hat{D}_0$ in terms of single-particle wave functions φ_α can be evaluated with standard methods of many-body theory [40]. The static structure factors at finite T for a unit cell in Eq. (17) become

$$S^{(0)}_{\mathrm{el},t}(\boldsymbol{q}) = \frac{1}{N_t}\mathrm{tr}\{\hat{F}_t(-\boldsymbol{q})\hat{D}_0\hat{F}_t(\boldsymbol{q})\hat{D}_0\}$$
$$= \frac{1}{N_t}\left|\sum_\alpha w_\alpha \langle\varphi_\alpha|e^{i\boldsymbol{q}\cdot\boldsymbol{r}}\hat{T}_t|\varphi_\alpha\rangle\right|^2, \quad (22a)$$

$$S^{(0)}_{\mathrm{inel},tt'}(\boldsymbol{q}) = \frac{1}{N_t}\mathrm{tr}\{\hat{F}_{tt'}(-\boldsymbol{q})(1-\hat{D}_0)\hat{F}_{t't}(\boldsymbol{q})\hat{D}_0\}$$
$$= 1 - \frac{1}{N_t}\sum_{\alpha,\beta} w_\alpha w_\beta |\langle\varphi_\alpha|e^{i\boldsymbol{q}\cdot\boldsymbol{r}}\hat{T}_{tt'}|\varphi_\beta\rangle|^2, \quad (22b)$$

$$w_\alpha = \frac{1}{1+e^{-\varepsilon_\alpha/T}}, \quad (22c)$$

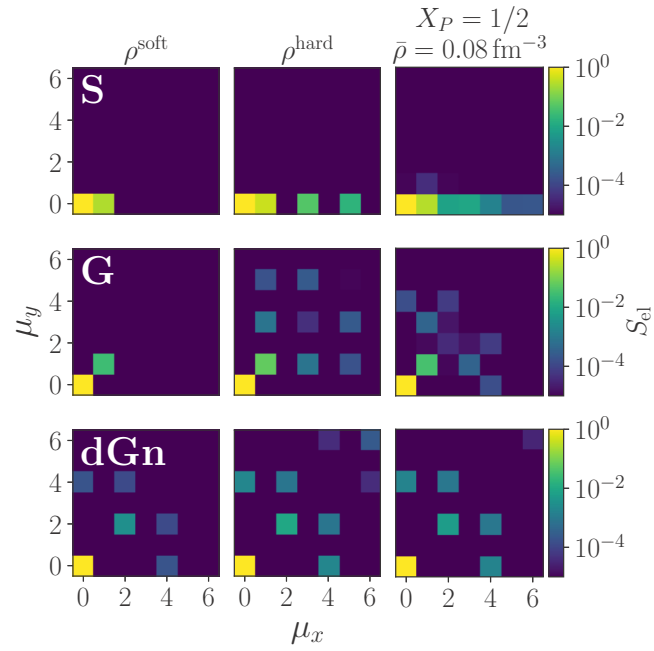

FIG. 2. First components of the elastic structure function in the x-y plane. The μ_x and μ_y label the Fourier bins in x and y directions. The upper row shows slab, middle gyroid, and lower double gyroid networklike configurations. The first column displays the smooth model (2a), the second column is the hard model (2b), and the third column is the actual pasta configuration (neutrons) from DFT calculations with proton fraction $X_P = 1/2$ and average density $\bar{\rho} = 0.08$ fm^{-3}.

where w_α is the thermal occupation probability of the single-particle state φ_α.

III. RESULTS

A. Elastic structure factor

The elastic structure factor is proportional to the normalized absolute square of the Fourier transform of the particle density. The model structures (1) indicate that the different geometries should be distinguished by marked difference in the distribution of these Fourier components. This surely holds for three-dimensional (3D) distributions before angular averaging. This is shown in Fig. 2, which shows the first six Fourier coefficients of the first quadrant in the μ_x-μ_y plane of the elastic structure function for S, G, and dGn geometries. In the left column the densities are modeled after the "soft" approximation (2a) and the second column shows the result for the "hard" approximation (2b). Finally, the third column shows results from realistic, self-consistent 3D simulations of the pasta configurations at $T = 0$.

The soft approximation shows already the leading peaks of the elastic structure function. In fact, the distribution and predominance of Fourier components can be read off from the analytical structures in Eqs. (1). This is straightforward for the single configurations and a bit more involved for the double configurations because they contain the absolute value [Eqs. (3)]. Complementing Fig. 2, we list in Table II the first

TABLE II. First dominant peak(s) in the elastic structure factor $S_{\rm el}$ for the different pasta configurations.

Sshape	$\lvert\boldsymbol{\mu}\rvert$	$\boldsymbol{\mu}$	
S	1	(±1,0,0)	
P	1	(±1,0,0)	and permutations
G	$\sqrt{2}$	(±1, ±1,0)	and permutations
D	$\sqrt{3}$	(±1, ±1, ±1)	
dG	$\sqrt{6}$	(±2, ±1, ±1)	and permutations
	$\sqrt{8}$	(±2, ±2,0)	and permutations

dominant peaks for all configurations considered in this work, and here for all three directions in **k** space.

The hard distribution, middle column in Fig. 2, shows already secondary peaks, because the steep transition at the surface enhances higher Fourier components. Note that the single configurations in this model occupy only peaks with odd μ_i (except for $\boldsymbol{\mu} = 0$) while double configurations can occupy all $\boldsymbol{\mu}$. The self-consistent DFT pasta configurations (right panels) occupy all Fourier coefficients. For the slab shape, S, almost exclusively the coefficients in x direction are occupied, because the configuration is homogeneous in the other two directions. One can spot only very small disturbances into other directions due to spatial fluctuations in the calculations. The gyroid as well as the double gyroid are very close to the hard configurations.

Pasta matter in the stellar environment will appear as an isotropic distribution of finite fragments of nuclear matter. This suggests that we are now looking at angular averaged distributions which are radial distributions in momentum space. In the following, we concentrate on the structure functions for density $\rho = 0.04\ \mathrm{fm}^{-3}$ and proton fraction $X_P = 1/3$, which already contain all features found at other densities and/or proton fractions. For completeness, we provide results for a higher value of the density, $\rho = 0.08\ \mathrm{fm}^{-3}$, and for proton fraction $X_P = 1/2$ in the Supplemental Material [41].

Figure 3 shows the elastic structure factor as function of the momentum transfer q for $\rho = 0.04\ \mathrm{fm}^{-3}$ and proton fraction $X_P = 1/3$. It is striking that the first peak appears for all different configurations at about the same value, $q = 0.31\ \mathrm{fm}^{-1}$, although the peaks are at very different bins in Fourier space (compare to Fig. 2 and Table II). For comparison we also show the first few possible q bins according to the box lengths $q_{\rm bin} = \frac{2\pi}{L}|\boldsymbol{\mu}|$. It seems that the peak number in Fourier space is counterweighted by the cell size of the geometry, delivering eventually all first maxima at about the same q value. However, the further evolution of peaks with their fine structure is sensitive to the exact pasta configuration.

Proton and neutron peak structures are very similar, also for a proton fraction of $X_P = 1/10$. The most important difference is that the proton distribution decays more slowly with large q, because the protons are more localized for $X_P < 1/2$ while the neutrons form a neutron skin, sometimes even a finite background gas.

We have also checked the impact of proton content X_P and of temperature T. It turns out that the trends are very similar in all geometries. Thus we restrict the analysis here to the

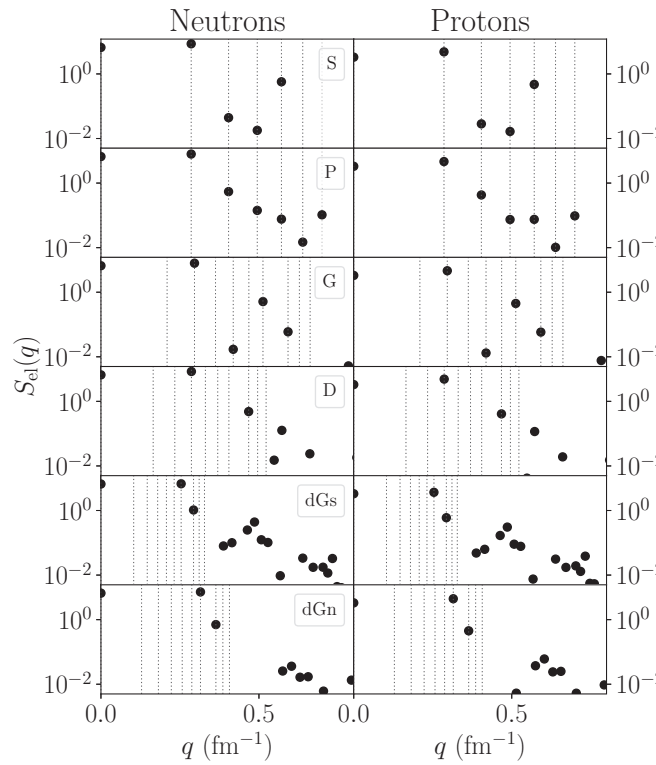

FIG. 3. Angular averaged elastic structure factor for all studied pasta configurations for $\rho = 0.04\ \mathrm{fm}^{-3}$ and $X_P = 1/3$. Left panels: neutrons; right panels: protons. Additionally, the first possible bins, up to $\boldsymbol{\mu}^2 = 10$, are shown.

slab geometry. Figure 4 shows the elastic structure factors for the slab shape at different temperatures and proton fractions. The position of the first peak moves with increasing proton fraction and temperature. Its trend is closely related to box size: the smaller the box the higher the q of the peak. The preferred box lengths for the slabs were studied in a previous paper [35]. They become larger for smaller proton fractions. The box lengths increase for $T = 2\ \mathrm{MeV}$ and decrease for higher temperatures.

The slab shape is homogeneous in two directions and has only nonzero contributions in one direction. The peak structure is relatively simple, being equidistant in q. The only exception is the slab at $T = 0$ and $X_P = 1/3$, where small additional peaks show up, which happens because there are some fluctuations into the other two directions.

The single peaks are decreasing in magnitude for larger q values, which is typical for form factors. This trend becomes stronger for smaller proton fraction and higher temperature. This is due to stronger smoothing of the surfaces and it is especially visible for neutrons, which form a neutron background gas for high temperatures or small proton fractions.

B. Inelastic structure factor

In contrast to the elastic structure factor, the inelastic structure factor is a smooth function also for strictly periodic systems, because it is sensitive to the detailed wave functions and these wave functions are only quasiperiodic (Bloch states).

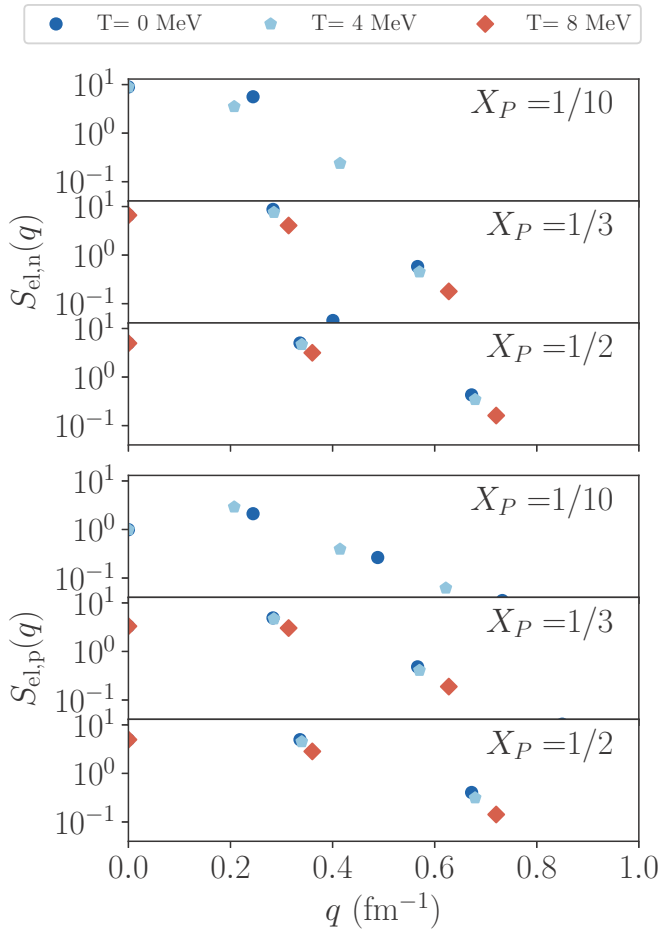

FIG. 4. Elastic structure factor for the slab shape at $\rho = 0.04$ fm^{-3} for different temperatures and proton fractions.

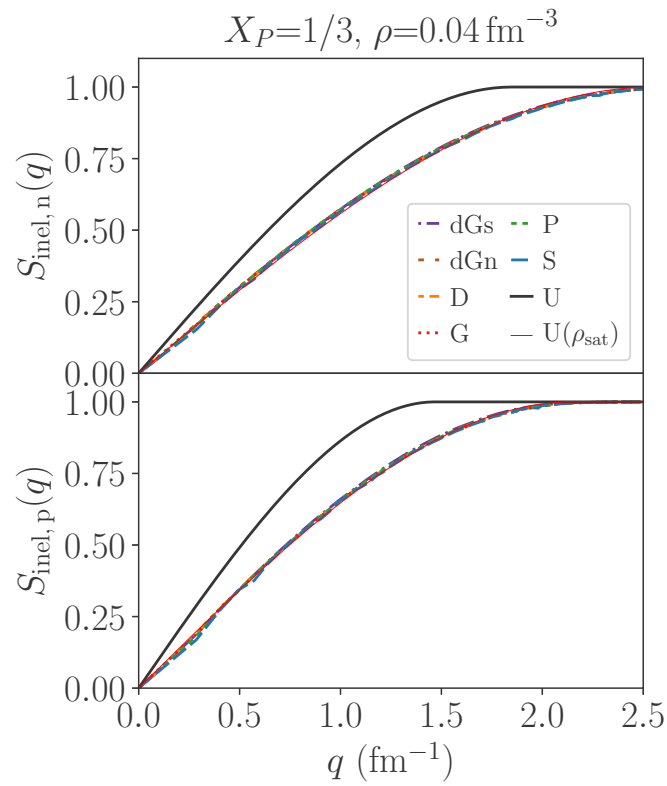

FIG. 5. Inelastic structure factor for all pasta configurations (dashed lines) and uniform matter with the same mean density (thick solid line) as well as uniform matter with saturation density in the pasta solid phase (thin solid line). Upper panel: neutrons; lower panel: protons.

Figure 5 shows the inelastic proton and neutron structure factors for all studied pasta configurations for $X_P = 1/3$ and $\rho = 0.04$ fm^{-3} compared with the one for uniform matter. First, it turns out that the structure factors are identical for all pasta configurations, except for a small deviation stemming from finite-size effects. However, compared to uniform matter at the same mean density (heavy black line labeled U), the inelastic structure factors are reduced. However, considering uniform matter having the density ρ_{sat} which is found inside the high density pasta phase [small red line denoted U(ρ_{sat})], we find practically the same pattern as for the pasta structures. There is a one-to-one correspondence to saturation density ρ_{sat}. The reason is that the inelastic structure factor in DFT only reflects the Pauli correlation in the filled volumes of the pasta configurations. Higher correlations are not included. Real two-particle correlations can be resolved by other methods like molecular dynamics (MD) [20,21,25]. However, in MD simulations the Pauli exclusion principle is not strictly reproduced, as a phenomenological potential is implemented to simulate the effect. To include both Pauli effects as well as higher many-particle correlations, it would be necessary to perform random phase approximation (RPA) calculations [30,31,33] or use Monte Carlo methods [32].

Figure 6 shows the neutral-current, inelastic structure factors for varying temperatures and proton fractions. The simulated results shows occasionally small wiggles in the proton structure factors at zero temperature. These are caused by fluctuations from finite particle numbers in the box which are unimportant for our discussion. The $T = 0$ results are the same as those shown before where, again, the slab results are smaller than the trend from homogeneous matter (when compared at same average density). This difference decreases with increasing temperature, because the simulated slab acquires an increasingly softer surface and slowly approaches homogeneous matter. For $X_P = 1/10$ the structure factor of neutrons for the slab is already very close to uniform matter due to the large neutron background density. In contrast, the proton structure factors for slabs and uniform matter differ significantly. The trend of the inelastic structure factors at $\boldsymbol{q} = 0$ with temperature deserves a comment. The value $S_{\mathrm{inel},tt}(0)$ starts at zero for $T = 0$, which expresses the Pauli principle between two like nucleons. The value increases with temperature, because higher momenta in phase space are becoming occupied and lower momenta in phase space are becoming unoccupied such that the Pauli blocking is reduced. The effect is independent of the spatial profile of matter.

Figure 7 shows the charged-current structure factors. We see that the differences of the slab to uniform matter are comparable to those for the neutral-current structure factors.

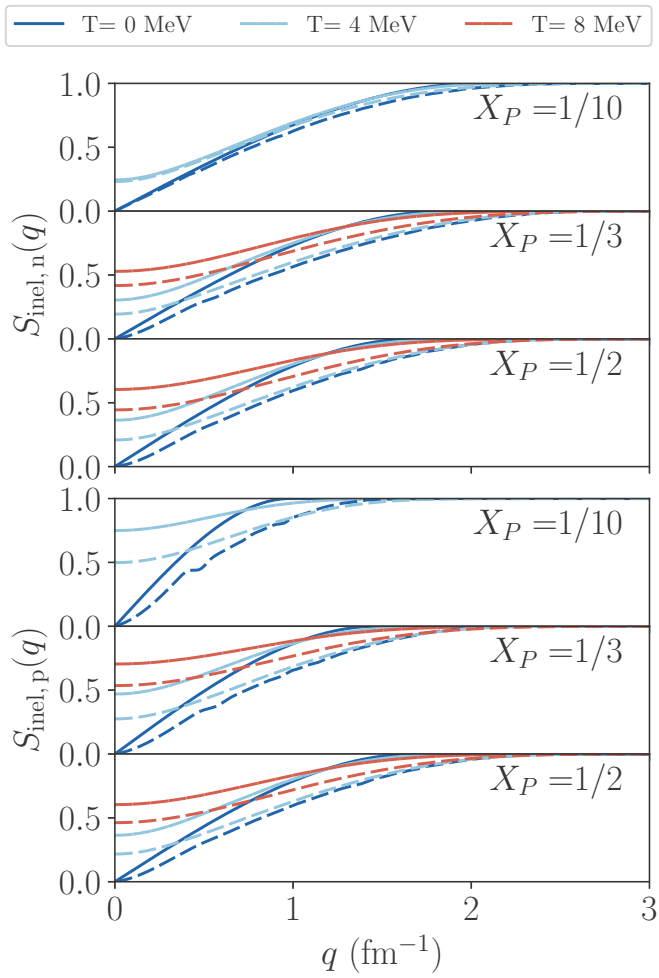

FIG. 6. Inelastic structure factor for the slab shape (dashed lines) for $\rho = 0.04$ fm^{-3} at different temperatures and proton fractions in comparison to uniform matter (solid lines).

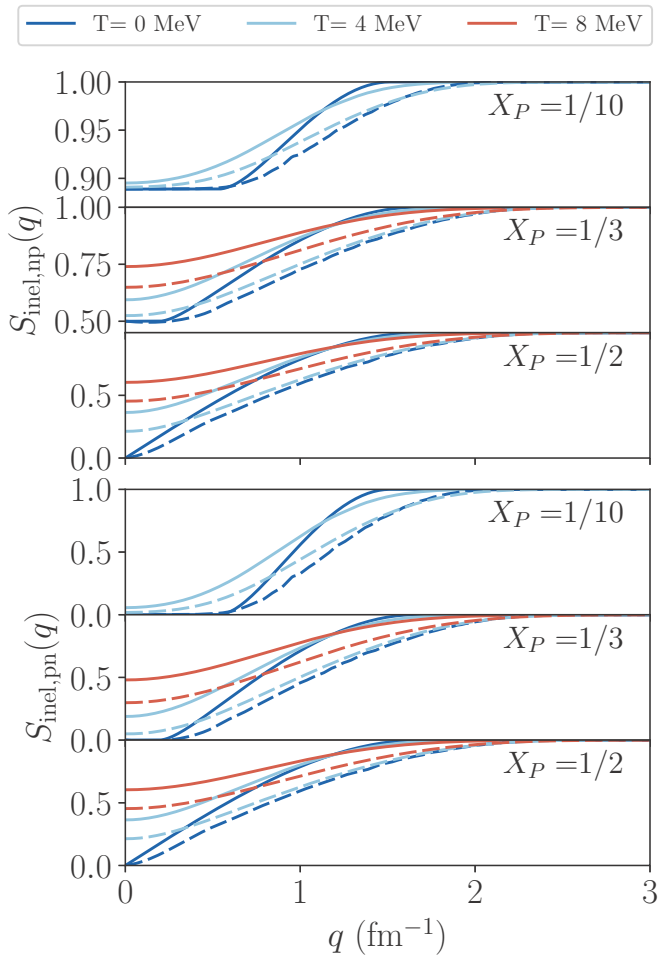

FIG. 7. Charged-current inelastic structure factors for the slab shape (dashed lines) for $\rho = 0.04$ fm^{-3}, at different temperatures and different proton fractions, in comparison to uniform matter (solid lines).

Though, the overall behavior is a bit different. While for $X_P < 1/2$ for $p \to n$ reactions the structure factor starts to increase for higher values of q, the structure factor for $n \to p$ starts at $q = 0$ with a nonzero value and increases with a lower slope. At low temperatures, again, the difference between homogeneous matter and pasta is more pronounced.

C. Impact on neutrino opacity

Finally, we are going to estimate the impact of nuclear pasta matter on the neutrino opacity. To that end we only consider neutral-current reactions, because, as we have seen in the previous sections, pasta matter has only a marginal influence on charged-current reactions, because there is no elastic scattering channel.

The upper panel of Fig. 8 shows the averaged static vector structure factors for neutrons for $\rho = 0.04$ fm^{-3} and $X_P = 1/3$. This structure factor has the most impact on opacity, because it contains the elastic part. The vector static structure factors for protons also contain an elastic contribution; however, it is strongly suppressed through the small coupling constant $c_{V,p}$. The different pasta configurations all show peaks at approximately the same position and same heights. Only the double gyroid configurations deviate slightly.

The lower panel of Fig. 8 shows the resulting opacity. While for low neutrino energies pasta matter slightly reduces the opacity, it enhances it for neutrino energies larger than 25 to 30 MeV. Note that the impact seems to be lower than in Ref. [20], because we also take into account the contribution from the axial current.

Figure 9 shows the same quantities as Fig. 8 but only for the slab, as representative of all pasta configurations, and for uniform matter, both for a series of different temperatures. We expect that the other geometries show behavior similar to the slab configuration, since we have seen already at zero temperature that all geometries behave very similarly. Finite temperature should even reduce the difference between the different pasta shapes, because the density profiles are washed out. Slab configurations show a pronounced peak in the structure factor and subsequently a significant enhancement in opacity between 30 and 50 MeV. The effect is largest at zero temperature. Figure 10 compares the mean opacity for slab and uniform matter as functon of temperature for a series

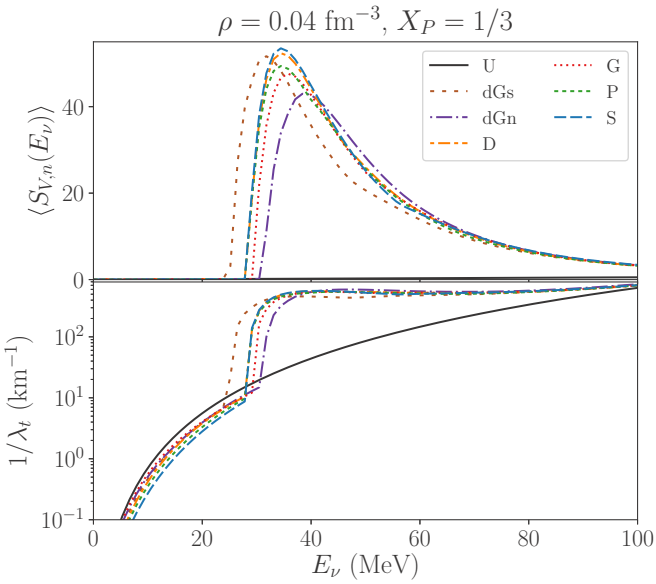

FIG. 8. Averaged vector static structure factors for neutrons (upper panel) and opacity (lower panel) for $\rho = 0.04$ fm^{-3} and $X_P = 1/3$ for different pasta configurations and uniform matter.

of proton fractions X_P. While for symmetric nuclear matter ($X_P = 1/2$) the impact of slab structure is rather small, it becomes larger for smaller proton fractions. This is because for smaller proton fractions the elastic peak is shifted to lower neutrino energies (cf. Fig. 4) and thus has a larger overlap with the neutrino energy distribution already at lower temperatures. For $X_P = 1/10$ the impact of pasta matter is significant and enhances the opacity by a factor of about 3 at a temperature of 4 MeV.

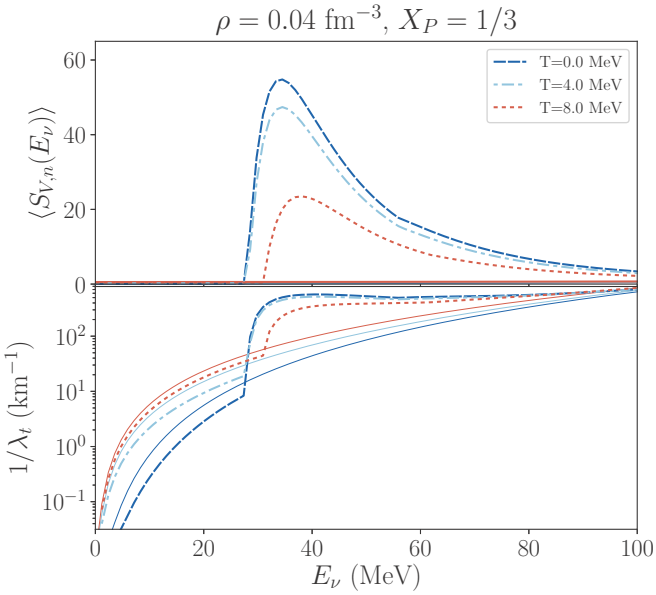

FIG. 9. Same as Fig. 8 but only for the pasta slab configuration (dashed) and for uniform matter (solid) and varying temperatures.

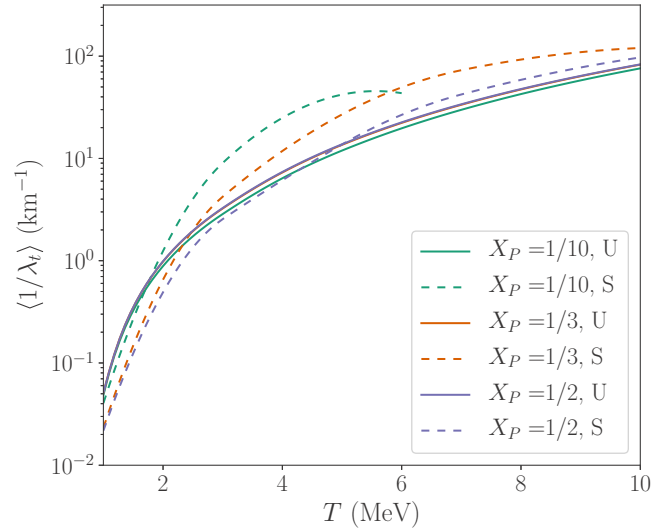

FIG. 10. Neutrino opacities for the pasta slab configuration and uniform matter with respect to the temperature for $\rho = 0.04$ fm^{-3} at three different proton fractions.

In Ref. [22], a similar analysis has been performed in the framework of molecular dynamics (MD). The results are qualitatively similar, especially regarding the position of the onset of the peak in the structure factor. The heights of the peaks are in the same order, also for the cases where completely different configurations were considered.

IV. CONCLUSIONS

We calculated the elastic and inelastic parts of the structure factor for nuclear pasta configurations and for uniform matter. This was done at a fully quantum mechanical level using nuclear density-functional theory (DFT). All considered pasta configurations appear in a cubic, periodic lattice with lattice spacing (box length) depending on the structure. The analysis was complemented by a simple analytical model of the minimal surfaces corresponding to the most important pasta structures: slab (S), primitive (P), gyroid (G), and diamond (D). Unlike uniform matter, the different pasta configurations produce an elastic structure factor with a rich and distinctive pattern.

The elastic structure factor is a function of transferred momentum. Periodic lattice structure produces distinctive peaks at the reciprocal vector of the lattice. The pasta configuration determines box lengths (length of the elementary cell) and distributions of strength over the peaks. The emerging pattern depends sensitively on the pasta configuration. Nonetheless, the first dominant peak shows up at roughly the same momentum transfer for all configurations. Changes in box length, thus lowest momentum bin, are compensated by the fact that the first dominant peak appears at different bin number for different configurations. The similarity of dominant transferred momentum means that the overall trend for the elastic structure is similar for all configurations. Only details change with the changing configuration.

There are unique trends with changing proton fraction and temperature. Lower proton content shifts the peaks to lower momentum transfer q. High temperatures $T > 4$ MeV shift the peaks to higher momentum transfer q and the peaks decrease then more rapidly with higher q because the matter is smoothed and approaches uniform matter.

The inelastic structure factor is found to be independent of the actual pasta configuration and it is the same as uniform matter at a density which corresponds to the saturation density in the filled regions of pasta structures. It is only this saturation density which counts. This happens because in DFT the inelastic structure factor only reflects the Pauli correlations, as one can also see from the fact that the structure factors at temperature zero are exactly zero, while finite temperature which overrides gradually the Pauli blocking allows for a nonvanishing inelastic structure factor at $q = 0$.

Finally, we computed the neutrino opacities for the given structures as a function of temperature and proton fraction. The results do not depend much on the actual structure, but differ significantly from uniform matter, particularly at low temperature and low proton fraction. Pasta structures enhance the neutral-current opacity up to a factor of 4. For charged-current opacity the effect of pasta is minor.

In summary, nuclear pasta has a noticeable impact on the structure factors and thus on inelastic and elastic neutrino scattering. While for inelastic reactions the cross section is reduced, the elastic coherent scattering increases dramatically. The effect can be of importance for the cooling of neutron stars as well as for core-collapse supernova models.

ACKNOWLEDGMENTS

Computational resources were provided by the Center for Scientific Computing (CSC) of Goethe University Frankfurt. This work has been funded by the Deutsche Forschungsgemeinschaft (DFG, German Research Foundation), Project No. 279384907–SFB 1245.

[1] D. G. Ravenhall, C. J. Pethick, and J. R. Wilson, Phys. Rev. Lett. **50**, 2066 (1983).
[2] M. Hashimoto, H. Seki, and M. Yamada, Prog. Theor. Phys. **71**, 320 (1984).
[3] C. O. Dorso, P. A. Giménez Molinelli, and J. A. López, Phys. Rev. C **86**, 055805 (2012).
[4] M. E. Caplan, A. S. Schneider, and C. J. Horowitz, Phys. Rev. Lett. **121**, 132701 (2018).
[5] R. D. Williams and S. E. Koonin, Nucl. Phys. **435**, 844 (1985).
[6] M. Okamoto, T. Maruyama, K. Yabana, and T. Tatsumi, Phys. Rev. C **88**, 025801 (2013).
[7] H. Pais, S. Chiacchiera, and C. Providência, Phys. Rev. C **91**, 055801 (2015).
[8] P. Bonche and D. Vautherin, Nucl. Phys. A **372**, 496 (1981).
[9] P. Magierski and P.-H. Heenen, Phys. Rev. C **65**, 045804 (2002).
[10] P. Gögelein and H. Müther, Phys. Rev. C **76**, 024312 (2007).
[11] W. G. Newton and J. R. Stone, Phys. Rev. C **79**, 055801 (2009).
[12] H. Pais and J. R. Stone, Phys. Rev. Lett. **109**, 151101 (2012).
[13] B. Schuetrumpf, M. A. Klatt, K. Iida, J. A. Maruhn, K. Mecke, and P.-G. G. Reinhard, Phys. Rev. C **87**, 055805 (2013).
[14] B. Schuetrumpf, K. Iida, J. A. Maruhn, and P.-G. Reinhard, Phys. Rev. C **90**, 055802 (2014).
[15] B. Schuetrumpf, M. A. Klatt, K. Iida, G. E. Schröder-Turk, J. A. Maruhn, K. Mecke, and P.-G. Reinhard, Phys. Rev. C **91**, 025801 (2015).
[16] B. Schuetrumpf and W. Nazarewicz, Phys. Rev. C **92**, 045806 (2015).
[17] F. J. Fattoyev, C. J. Horowitz, and B. Schuetrumpf, Phys. Rev. C **95**, 055804 (2017).
[18] C. J. Horowitz and D. K. Berry, Phys. Rev. C **78**, 035806 (2008).
[19] J. A. Pons, D. Viganò, and N. Rea, Nat. Phys. **9**, 431 (2013).
[20] C. J. Horowitz, M. A. Pérez-García, and J. Piekarewicz, Phys. Rev. C **69**, 045804 (2004).
[21] C. J. Horowitz, M. A. Pérez-García, J. Carriere, D. K. Berry, and J. Piekarewicz, Phys. Rev. C **70**, 065806 (2004).
[22] H. Sonoda, G. Watanabe, K. Sato, T. Takiwaki, K. Yasuoka, and T. Ebisuzaki, Phys. Rev. C **75**, 042801(R) (2007).
[23] P. Grygorov, P. Gögelein, and H. Müther, J. Phys. G **37**, 75203 (2010).
[24] A. Roggero, J. Margueron, L. F. Roberts, and S. Reddy, Phys. Rev. C **97**, 045804 (2018).
[25] R. Nandi and S. Schramm, Astrophys. J. **852**, 135 (2018).
[26] S. Reddy, M. Prakash, and J. M. Lattimer, Phys. Rev. D **58**, 013009 (1998).
[27] C. J. Horowitz, Phys. Rev. D **65**, 043001 (2002).
[28] S. Cowell and V. R. Pandharipande, Phys. Rev. C **70**, 035801 (2004).
[29] A. Burrows, S. Reddy, and T. Thompson, Nucl. Phys. A **777**, 356 (2006).
[30] A. Pastore, D. Davesne, and J. Navarro, Phys. Rep. **563**, 1 (2015).
[31] A. A. Dzhioev and G. Martínez-Pinedo, EPJ Web Conf. **194**, 02006 (2018).
[32] G. Shen, S. Gandolfi, S. Reddy, and J. Carlson, Phys. Rev. C **87**, 025802 (2013).
[33] P. F. Bedaque, S. Reddy, S. Sen, and N. C. Warrington, Phys. Rev. C **98**, 015802 (2018).
[34] L. Riz, S. Gandolfi, and F. Pederiva, J. Phys. G: Nucl. Part. Phys. **47**, 045106 (2020).
[35] B. Schuetrumpf, G. Martínez-Pinedo, Md. Afibuzzaman, and H. M. Aktulga, Phys. Rev. C **100**, 045806 (2019).
[36] K. Michielsen and H. De Raedt, Phys. Rep. **347**, 461 (2001).
[37] J. Erler, C. J. Horowitz, W. Nazarewicz, M. Rafalski, and P.-G. Reinhard, Phys. Rev. C **87**, 044320 (2013).
[38] J. A. Maruhn, P.-G. Reinhard, P. D. Stevenson, and A. S. Umar, Comput. Phys. Commun. **185**, 2195 (2014).
[39] B. Schuetrumpf, P.-G. Reinhard, P. Stevenson, A. Umar, and J. Maruhn, Comput. Phys. Commun. **229**, 211 (2018).
[40] R. Balian, Y. Alhassid, and H. Reinhardt, Phys. Rep. **131**, 1 (1986).
[41] See Supplemental Material at http://link.aps.org/supplemental/10.1103/PhysRevC.101.055804 for additional results for varied density and proton fractions.